RSC Advances

PAPER

View Article Online
View Journal | View Issue

Cite this: *RSC Adv.*, 2023, **13**, 9448

Visible light antibacterial potential of cement mortar incorporating Cu-ZnO/g-C_3N_4 nanocomposites

Xiaomin Liu,[a] Zhengxian Yang,*[ab] Kang Li,[b] Bruno Briseghella,[b] Giuseppe Carlo Marano[c] and Jiankun Xu[b]

Received 28th December 2022
Accepted 20th February 2023

DOI: 10.1039/d2ra08281k

rsc.li/rsc-advances

In this work, a hybrid Cu-ZnO/g-C_3N_4 nanocomposite was synthesized and introduced to fabricate photocatalytic cement mortars by internal mixing. The bactericidal properties of the photocatalytic mortars were explored by using *E. coli*, *S. aureus* and *P. aeruginosa* as a bacteria test strain. The results showed that the Cu-ZnO/g-C_3N_4 nanocomposite had an enhanced harvesting of visible light energy and exhibited excellent stability during the photocatalytic process, which favored a long-term usage performance. The sterilizing efficiency of the photocatalytic cement mortars improved with an increasing content of Cu-ZnO/g-C_3N_4 nanocomposites. A possible bactericidal mechanism was proposed based on the active species trapping experiments, verifying that the photogenerated holes (h^+) and $^{\bullet}O_2^-$ radicals were the main active species.

1. Introduction

Coastal and offshore concrete structures such as cross-sea bridges, port wharfs and subbottom tunnels, exposed directly or indirectly to the marine environment are prone to deterioration and premature failures due to biofouling induced corrosion. It is known that the inherent porous structure of concrete creates a favorable environment for microbial colonization.[1] In the microorganisms corroding concrete, the dominant microorganisms are sulfur bacteria, commonly known as sulfur-oxidizing bacteria (SOB). It can oxidize sulfur alone or sulfur-containing substances into biological sulfuric acid.[2] The biogenic acids and other metabolites produced by the organisms can cause significant internal or external damage to the concrete structure, resulting in performance deterioration, increased porosity and decreased durability.[3] Thanks to advances in photocatalysis science technology, as well as in nanotechnology, it is feasible to make photocatalytic cementitious materials by introducing appropriate photocatalysts for disinfection of bacteria.[4,5] It's worth noting that cementitious materials can immobilize photocatalyst powders in their matrices due to its strong binding properties. Furthermore, the porous structure of the hardened cement composites helps the incorporated photocatalyst particles to come into bind with the target objects to facilitate the photocatalytic conversion.[6]

Among inorganic semiconducting materials, ZnO has been widely used as an effective photocatalyst due to its low cost, eco-friendliness, high electron mobility, stability and high quantum yield properties. In addition, ZnO can be used as nanomaterials to fill the internal pores of cement-based materials, which greatly improves the mechanical properties and durability of cement-based materials, and gives buildings the intelligence and versatility they do not possess.[7] However, the large bandgap of ZnO restricts the light absorption to UV region which accounts for only 5% of the solar spectrum.[8] For this reason, some suitable approaches have been invented to moderate its bandgap and inhibit the recombination rate of the generated charge carriers, while bring its absorption in the visible region. Studies have shown that elemental doping of ZnO and heterojunction formation with proper semiconductors help overcome its limitations and maximize its visible light absorption.[9,10] Metals doped ZnO photocatalyst were found to be effective to shift the optical absorption towards distributed wavelength and thus increased the photocatalytic activity.[11] As a polymeric semiconductor, g-C_3N_4 has appealed to the researchers because of its distinctive properties like modifiable electronic structure, stability, and visible light activity. In addition, g-C_3N_4 has a layered structure similar to graphite, which is more stable and more compatible with building materials than other conventional photocatalytic materials.[12] However, the usage of g-C_3N_4 as a single photocatalyst is constricted due to its limited visible light absorption and rapid recombination of the photogenerated electro–hole pairs (e–h).[13] So, as a single component photocatalyst, the photocatalytic antibacterial proficiency of g-

[a]*School of Advanced Manufacturing, Fuzhou University, Quanzhou 362200, China. E-mail: zxyang@fzu.edu.cn; zhengxian.yang@gmail.com*

[b]*Joint International Research Laboratory of Deterioration and Control of Costal and Marine Infrastructures and Materials, College of Civil Engineering, Fuzhou University, Fuzhou 350108, China*

[c]*Department of Structural, Geotechnical and Building Engineering, Politecnico di Torino, Corso Duca degli Abruzzi, 24-10129 Torino, Italy*

C_3N_4 is not practical. Hence, many methods have been developed to deal with these challenges. The appropriate construction of a ZnO/g-C_3N_4 nanocomposite has the potential to contribute synergistic benefits over that of individual g-C_3N_4 and ZnO in terms of photocatalytic performances, especially the improved visible light activity. Wang *et al.* found that the photodegradation effect of the honeycomb ZnO/g-C_3N_4 heterostructure on Rhodamine B is better than that of the original g-C_3N_4 under visible light.[14] Jo and Selvam reported that the photocatalytic degradation performance of core–shell g-C_3N_4/ZnO composites for phenol is better than that of original g-C_3N_4.[15] Nevertheless according to our literature research, little study has yet been reported for introducing ZnO/g-C_3N_4 into cementitious materials with regard to photocatalytic sterilization.

In this work, groups of Cu-ZnO/g-C_3N_4 nanocomposites were prepared with different contents of g-C_3N_4. The photocatalytic inactivation property and sterilization mechanism of the Cu-ZnO/g-C_3N_4 nanocomposites toward *E. coli*, *S. aureus* and *P. aeruginosa* were investigated, while the microstructure, morphology, and optical properties were characterized by X-ray diffraction (XRD), field emission scanning electron microscopy coupled with energy-dispersive X-ray spectroscopy (SEM-EDS), X-ray photoelectron spectroscopy(XPS), Fourier transform infrared spectra (FT-IR), UV-vis diffuse reflectance spectrum (UV-vis DRS) and photoluminescence (PL). Furthermore, a series of cement mortars were fabricated with the introduction of Cu-ZnO/g-C_3N_4 by varying the content from 0.6 to 1.8 wt%. The photocatalytic performance of the mortars was evaluated by the real-time disinfection of *P. aeruginosa* under continuous visible light irradiation.

2. Experimental

2.1. Materials

$Zn(NO_3)_2\cdot 6H_2O$, $Cu(NO_3)_2\cdot 3H_2O$, urea ($CO(NH_2)_2$), sodium citrate dihydrate ($Na_3C_6H_5O_7\cdot 2H_2O$, melamine ($C_3H_6N_6$), isopropanol, *p*-benzoquinone, sodium oxalate, ethanol, yeast extract, and tryptone were purchased from National Medicine Group Chemical Reagent Co., Ltd., China. *E. coli*, *S. aureus* and *P. aeruginosa* was obtained from First Institute of Oceanography, Ministry of Natural Resources. The 42.5-grade ordinary Portland cement (OPC) confirming Chinese national standard GB175-2007 is used. The chemical compositions of the OPC was measured by X-ray fluorescence (XRF) and shown in Table 1.

2.2. Synthesis of Cu-ZnO/g-C_3N_4 nanocomposites

The g-C_3N_4 was synthesized according to a previous report.[16] Typically, 15 g melamine was put into a crucible with a cover and heated to 550 °C for 4 h with a heating rate of 1 °C min^{-1} in a muffle furnace. After cooling to room temperature at the same rate, the yellow product was obtained.

For synthesis of Cu-ZnO/g-C_3N_4,[17] 0.23 g g-C_3N_4 powder was firstly dispersed in 70 ml of deionized water and sonicated for 45 min at 30 °C. Then, 1.036 g $Zn(NO_3)_2\cdot 6H_2O$, 0.051 g $Cu(NO_3)_2\cdot 3H_2O$, 0.42 g $CO(NH_2)_2$ and 0.103 g $Na_3C_6H_5O_7\cdot 2H_2O$ were dissolved in the above suspension under magnetically stirring for 60 min. The resulting mixture was transferred to a Teflon-liner wrapped in a stainless-steel autoclave and heated at 120 °C for 6 h. The precipitate was washed thoroughly with deionized water and anhydrous ethanol before being dried at 65 °C for 24 h. Then, the precipitate was transferred into a crucible with a lid and heated to 300 °C for 2 h at a heating rate of 2 °C min^{-1}. Finally, the powders were collected from the crucible after cooling down to room temperature. Similarly, pure ZnO, Cu-ZnO, ZnO/g-C_3N_4 was prepared at ambient conditions for comparison.

2.3. Preparation of photocatalytic cement mortars

For the preparation of photocatalytic cement mortars, all batches were prepared with a constant mix proportion of water : cement : sand is 0.5 : 1 : 3 by mass. A series of cement pastes were prepared with various contents of Cu-ZnO/g-C_3N_4 (0, 0.6, 1.2 and 1.8% by mass of cement). The specific procedure was operated as follows: the Cu-ZnO/g-C_3N_4 suspensions were firstly prepared by dispersing the corresponding proportion of Cu-ZnO/g-C_3N_4 into deionized water under ultrasonication for 15 min. Then, the dry cement was added and mixed at a low speed for 30 s. The sand (standard sand in compliance with IOS standards) was added subsequently and stirred for another 4 min (low speed for 120 s and high speed for 120 s). Finally, the fresh cementitious composites were cast into molds (Ø50 mm × 100 mm) with compaction on a vibration table. The samples were then cured in an environmental chamber for 28 days with a temperature of 20 ± 2 °C and 98% relative humidity before subjecting to assigned tests. The mortars with various contents of Cu-ZnO/g-C_3N_4 were labeled as CM-0, CM-0.6, CM-1.2 and CM-1.8. The cylinder specimens from each batch was cut into 10 mm thickness discs and used as test samples to examine the photocatalytic activities.

2.4. Characterization and measurements

The synthesized samples were characterized by various techniques to evaluate their properties and morphological differences. The structural features of the synthesized photocatalysts were characterized by X-ray diffraction (XRD) with an X-ray diffractometer (MiniFlex 600, Rigaku, Japan) at a scanning rate of 10° min^{-1}. The morphology of the samples was investigated by SEM (TECNAI G2 F20, FEI, USA). The functional groups and chemical bonds were measured by FTIR spectroscopy (AVATAR360, FEI, USA) in the scanning range of 4000–400 cm^{-1}. The electronic states of the g-C_3N_4, ZnO, Cu-ZnO and Cu-ZnO/g-C_3N_4 were analyzed by X-ray photoelectron spectroscopy (AXIS ULTRA DLD, Kratos, UK) with Al Kα radiation (1486.71 eV). The optical absorbance was studied by a UV-vis spectrometer (Cary 7000, Agilent, USA) from 200 nm to

Table 1 Chemical composition of Portland cement (wt%)

Material	CaO	SiO_2	Al_2O_3	Fe_2O_3	MgO	K_2O	Na_2O	SO_3	Loss
Cement	62.36	22.6	4.41	3.92	2.98	0.45	0.42	2.38	0.48

800 nm using barium sulfate as the background. Photoluminescence (PL) spectra were determined by a fluorescence spectrometer (F-7000, Hitachi, Japan).

2.5. Bacterial strains and culture conditions

E. coli, *S. aureus* and *P. aeruginosa* were selected as model microorganism for photocatalytic bactericidal investigation. Normally, the bacteria was incubated in a LB nutrient solution at 37 °C for 12 h with shaking at 150 rpm. To eliminate broth medium, the bacteria were separated by centrifuging at 5000 rpm for 8 min followed by washing several times using sterilized phosphate buffer solution (PBS, 0.01 M, and the pH is 7.4). The collected cells were diluted to the desired concentration in PBS. The spread plate method was used to estimate the number of bacteria, and the final suspension concentration was around 2–5 $\times$ 10^6 colony forming units (cfu ml^{-1}). All apparatus and materials were sterilized in an autoclave at 121 °C for 20 min prior to experiments.

2.6. Photocatalytic inactivation of bacteria

2.6.1. Bactericidal properties of g-C_3N_4, ZnO, Cu-ZnO, ZnO/g-C_3N_4 and Cu-ZnO/g-C_3N_4 composites. The photocatalytic experiments were carried out by using a 500 W Xe lamp as the light source with a 420 nm cutoff filter. Quartz glass test tube was used as the reaction vessel and the water was circulated in a jacket to maintain room temperature. The reaction system was magnetically stirred throughout the reaction. In this experiment, *E. coli* (4.6×10^6 cfu ml^{-1}), *S. aureus* (2.1×10^6 cfu ml^{-1}) and *P. aeruginosa* (2.6×10^6 cfu ml^{-1}) were used as model bacteria to evaluate the photocatalytic inactivation ability of the as-prepared photocatalysts. Blank control without photocatalysts and dark control with photocatalysts were also carried out. The amount of living bacteria was determined by the plate count method. Typically, 40 mg catalyst, 500 ml bacterial suspension and 49.5 ml phosphate buffered saline solution were added into quartz glass test tubes. After stirring magnetically in dark for 30 min to ensure an adsorption/desorption balance between the photocatalysts and bacteria, the suspension was exposed to light irradiation (1 W cm^{-2}). At given time intervals, 0.1 ml of the suspension was withdrawn and serially diluted with sterilized PBS. Then, 100 μl of the bacterial dilution was immediately spread on LB agar plates and incubated at 37 °C for 24 h to assess the number of viable cells. Three replicated plates were used for each incubation to verify the reproducibility of the results. For comparison, the blank control was performed in bacterial suspension under visible light irradiation without photocatalysts, and the dark control was carried out with photocatalysts and bacteria in dark. The survival rate was calculated according to the following equation: survival rate (%) = $(N_{survivor}/N_{control}) \times 100$, where $N_{control}$ and $N_{survivor}$ represent the numbers of viable cells in the blank control and after photocatalytic reaction, respectively. Therefore, the antibacterial rate was calculate: antibacterial rate (%) = 100 − survival rate.

2.6.2. Stability and reusability study. In order to verify the reusability and stability of the Cu-ZnO/g-C_3N_4 heterostructures, experiments were performed by repeating the photocatalytic sterilization of Cu-ZnO/g-C_3N_4 towards *P. aeruginosa* for seven successive times under the same operation condition. After every 60 min, the Cu-ZnO/g-C_3N_4 composites were gathered by centrifugation and washed with Milli-Q water and ethanol for a couple of times. After being dried, it was then reused in the following cycle. Besides, the changes in structure and morphology of Cu-ZnO/g-C_3N_4 after 7 cycles were characterized by XRD and FTIR.

2.6.3. Active species trapping experiments. The photocatalytic bactericidal mechanism was studied by active specie capture experiments. IPA (1 mM), BQ (1 mM) and sodium oxalate (1 mM) were used as scavengers to capture $^{\bullet}OH$, O_2^- and h^+, respectively. The photocatalytic antibacterial rates of *P. aeruginosa* were determined after the addition of scavengers into the photocatalytic reaction. The major active species in the photocatalytic process can be verified according to the change of photocatalytic antibacterial rate.[18]

2.6.4. Antibacterial experiment of photocatalytic cement mortars. The antibacterial performance of the photocatalytic cement mortars was investigated as the experimental setup depicted in Fig. 1. A 200 ml sandwich beaker was applied as the photocatalytic reactor for carrying out the disinfection experiment of *P. aeruginosa*. The mortar samples containing various content of Cu-ZnO/g-C_3N_4 were firstly autoclaved to sterilize it. Subsequently, the samples were soaked in 20 ml of *P. aeruginosa* suspension and kept in contact with bacteria environment under dark conditions for 15 min to reach adsorption desorption equilibrium. The 300 W Xe lamp (λ > 420 nm) was set at a distance of 35 cm to the surface of the suspension, and the whole reaction system was always kept at room temperature under the control of cooling water circulating machine. Other experiment steps were operated as in Section 2.6.1.

3. Results and discussion

3.1. Characterization of Cu-ZnO/g-C_3N_4 composites

3.1.1. XRD analyses. The XRD patterns of the prepared ZnO, Cu-ZnO, g-C_3N_4, ZnO/g-C_3N_4 and Cu-ZnO/g-C_3N_4 are shown in Fig. 2. As shown in Fig. 2, XRD pattern of g-C_3N_4 reveals two characteristic peaks. A weak peak appeared at 13.1° with crystal plane (100) is attributed to the inter-planar stacking peak of aromatic systems, while a strong peak at 27.4°, indexed

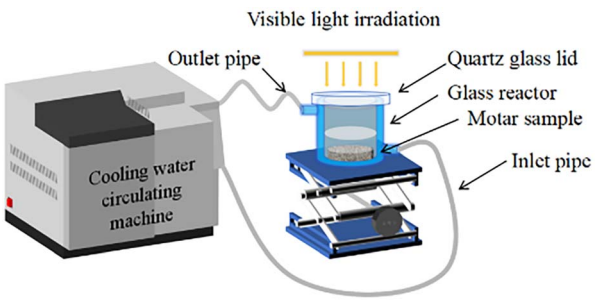

Fig. 1 Schematic diagram of the experimental setup for bacterial inactivation.

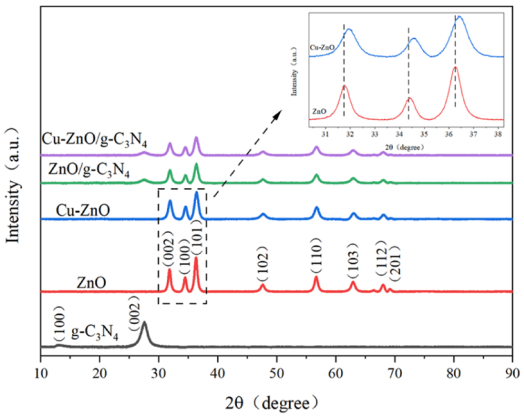

Fig. 2 XRD patterns of g-C_3N_4, ZnO, Cu-ZnO, ZnO/g-C_3N_4 and Cu-ZnO/g-C_3N_4 composites.

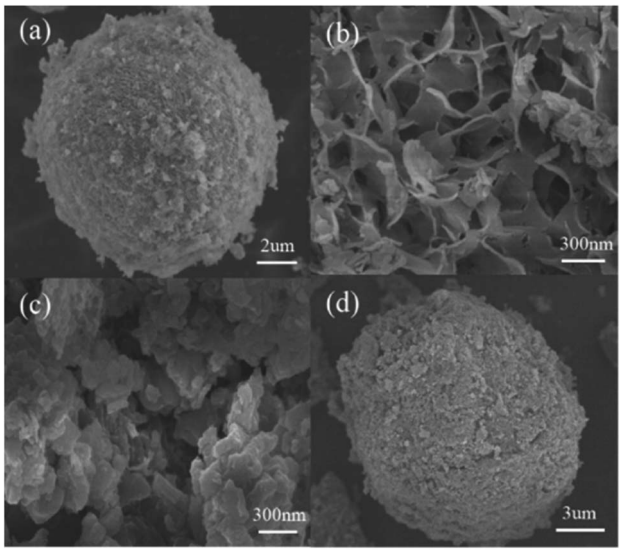

Fig. 3 SEM images of: (a and b) Cu-ZnO; (c) g-C_3N_4; (d) Cu-ZnO/g-C_3N_4 composites.

as (002) crystal planes corresponds to interlayer stacking of aromatic systems. The appearance of the strong and weak peaks at 27.4° and 13.1° endorses the formation of nanosheets in g-C_3N_4.[19] For ZnO, the recorded diffraction pattern validate that pure ZnO bear a hexagonal wurtzite structure with (100), (002), (101), (102), (110), (103), (112), and (201) crystal faces and can be entirely indexed to the standard pattern (JCPDS Card No. 36-1451).[20] Compared with the peaks in the XRD pattern of ZnO, the peaks corresponding to the synthesized Cu-ZnO composite are more broad and shift right slightly with a lower intensity, due to the incorporation of Cu^{2+} in ZnO.[21] This clearly indicates that Cu is successfully doped into the ZnO matrix. Because the ionic radius of Cu^{2+} (0.72 Å) is very similar to that of Zn^{2+} (0.75 Å), Cu could be easily embedded into the ZnO matrix *via* substitution of several Zn atoms in the matrix during preparation process.[21] Moreover, it is worth noting that the diffraction peak of g-C_3N_4 at 27.4° (002) exhibits low peak intensity in ZnO/g-C_3N_4 and Cu-ZnO/g-C_3N_4 composites, which is due to its low contents in the composites as compared to its pure form. The appearance of characteristic peaks of g-C_3N_4 and ZnO validates the successful formation of ZnO/g-C_3N_4 and Cu-ZnO/g-C_3N_4 composites. This observation reveals that the coupling of g-C_3N_4 sheets with the ZnO does not alter the morphology of g-C_3N_4 and ZnO, which is beneficial for photocatalytic action of the composite.[22,23]

3.1.2. SEM analyses. The morphology and microstructure of Cu-ZnO, g-C_3N_4 and the Cu-ZnO/g-C_3N_4 composites were explored by SEM. Fig. 3(a) and (b) show the morphology of synthesized Cu-ZnO samples, which possess hierarchical microsphere structures with an average diameter of 10 μm. These hierarchical microsphere structures contain large number of nanosheets which provides the porous and rough surface net-structure. As is reported, the surface holes are conducive to the capture and anchoring of bacteria, while the sharp Cu-ZnO nanosheets are used for mechanical sterilization.[24] As Fig. 3(c) shows, the g-C_3N_4 has an irregular two-dimensional (2D) layered structure agglomerated by numerous sheets. From Fig. 3(d), it can be seen that Cu-ZnO hierarchical microspheres is wrapped with g-C_3N_4 nanosheets, indicating the tightly contact between the Cu-ZnO and g-C_3N_4 which was favor for the migration of charge carriers in the interface of the Cu-ZnO and g-C_3N_4. It is found that doping Cu into ZnO and then coupling g-C_3N_4 tends to aggregate together and exhibits a uniform and regular 3D microsphere structure. In addition, the structure constructed between Cu-ZnO and g-C_3N_4 provides a suitable electronic heterojunction, greatly shortening the carrier migration distance and thus facilitating the photocatalytic reaction.

3.1.3. XPS analyses. XPS analysis was further utilized to analyze elemental states of Cu-ZnO/g-C_3N_4 and the obtained results were fitted by Gaussian multi-peak shapes. The full spectrum of Cu-ZnO/g-C_3N_4 and the fitted XPS spectra of Cu 2p, Zn 2p, O 1s, N 1s and C 1s were shown in Fig. 4. It can be seen that the Cu and Zn in the synthesized Cu-ZnO/g-C_3N_4 exhibit in the form of Cu^{2+} and Zn^{2+}, respectively. For the Zn 2p spectrum, Cu-ZnO/g-C_3N_4 exhibits two strong peaks at 1022.1 eV and 1045.2 eV; the former was attributed to Zn $2p_{3/2}$ and the latter was ascribed to Zn $2p_{1/2}$.[11] Similarly, the Cu $2p_{3/2}$ and Cu $2p_{1/2}$ peaks are found at binding energy of 933.41 eV and 953.17 eV. The O 1 s spectrum of Cu-ZnO/g-C_3N_4 presents two peaks at 530.5 eV and 532.5 eV. The peak located at 530.5 eV is attributed to the oxygen–metal bond in the crystal lattice, and the other one at 532.5 eV correspondsto O–H bond of H_2O absorbed on material surface. The N 1s spectra could be deconvoluted into three peaks, which correspond to the sp^2 hybridized nitrogen (N_{2C}), tertiary nitrogen (N_{3C}) and amino functional groups with H atom (N–H_x), respectively.[25] The fitted C 1s spectrum of Cu-ZnO/g-C_3N_4 shows three different peaks. Peaks at 288.1 eV are attributed to the carbon in N–C=N bond, and peaks at 284.9 eV are assigned to adventitious hydrocarbon from the XPS instrument itself. Another peak at 286.0 eV in C 1s spectra of Cu-ZnO/g-C_3N_4 is assigned to C–O bond, which comes from the combination C in g-C_3N_4 and O in ZnO (or Cu-ZnO). The

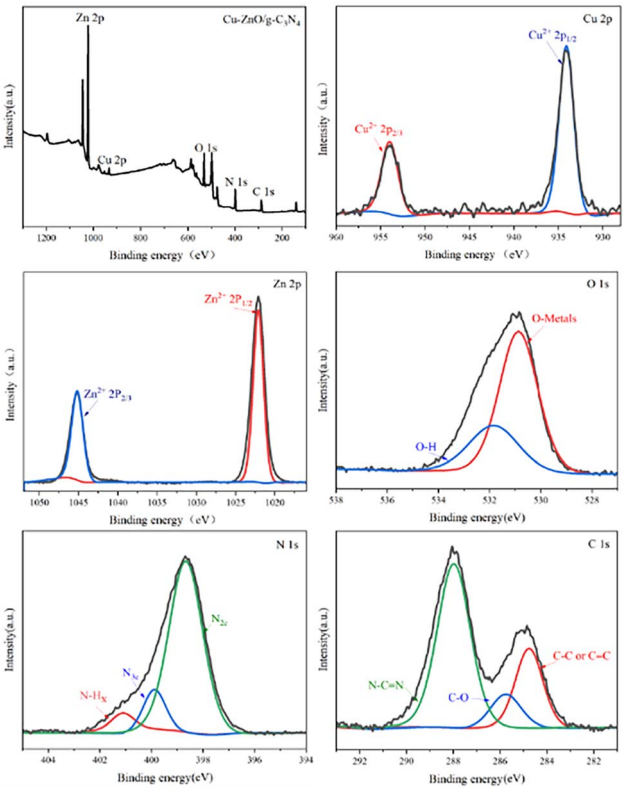

Fig. 4 Full XPS spectrum of Cu-ZnO/g-C_3N_4 and high-resolution XPS spectra of Cu 2p, Zn 2p, O 1s, N 1s and C 1s.

formation of C–O bond verifies that ZnO (or Cu-ZnO) and g-C_3N_4 are tightly connected *via* chemical bonding.[21]

3.1.4. FTIR analyses. Fig. 5 is the FTIR spectroscopy of ZnO, Cu-ZnO, g-C_3N_4, ZnO/g-C_3N_4 and Cu-ZnO/g-C_3N_4. As can be seen, the wide absorption bands at 3400 cm^{-1} exhibited in ZnO and Cu-ZnO can be attributed to the stretching mode of O–H groups likely due to the moisture presented in the samples. The two absorption bands, found in between 1380 cm^{-1} and 1420 cm^{-1} are referred to the bending vibrations of the O–H groups. The small absorption band observed at 838 cm^{-1} is

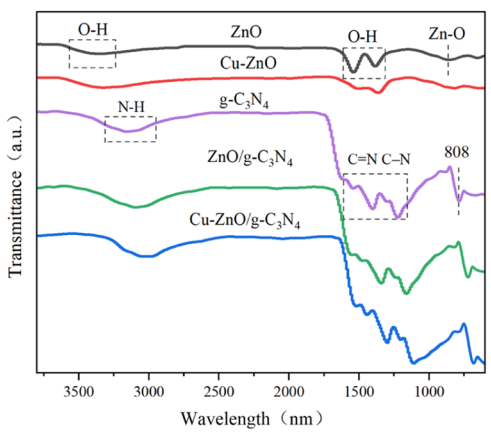

Fig. 5 FTIR spectra of the ZnO, Cu-ZnO, g-C_3N_4, ZnO/g-C_3N_4 and Cu-ZnO/g-C_3N_4 composites.

associated with Zn–O bending vibrational mode.[26] The peak at about 808 cm^{-1} is ascribed to the heptazine ring out-of-plane bending vibration mode. The broad band for N–H stretching vibration is observed from 2800 to 3400 cm^{-1}. The peaks in the range of 1200 cm^{-1}–1650 cm^{-1} are determined to be the stretching vibration of C=N double bond and C–N single bond of aromatic heterocycles.[27] The occurrence of the identical peaks in Cu-ZnO/g-C_3N_4 and ZnO/g-C_3N_4 validates the formation of the composites. Correspondingly, a small shift in absorption peaks of Cu-ZnO/g-C_3N_4 (approximately at 3083 cm^{-1}, 1615 cm^{-1}, and 1225 cm^{-1}) towards the lower wavenumber is observed compared to that of pristine g-C_3N_4 peaks. That variation in peaks authenticates the strong chemical interaction rather than simple physical interaction between the constituents of the heterostructure catalyst.[28]

3.1.5. UV-vis DRS analyses. The optical absorption characteristics of the ZnO, Cu-ZnO, g-C_3N_4 and Cu-ZnO/g-C_3N_4 were investigated by UV-vis DRS (Fig. 6(a)) and the band gap of the synthesized materials was estimated from the graph of $(\alpha h\nu)^2$ *versus* $h\nu$ (Tauc plot) for the absorption coefficient α that is related to the band gap E_g as $(\alpha h\nu)^2 = k(h\nu - E_g)$, where $h\nu$ is the incident light energy and k is a constant (Fig. 6(b)).[21] As in Fig. 6(a and b),the pristine g-C_3N_4 indicates an absorption edge at about 460 nm and its bandgap is estimated to be 2.70 eV, signifying its visible-light-induced photocatalytic activity mainly caused by the π–π^* transition. The absorption peak corresponding to ZnO is around 370 nm, with a bandgap of 3.20 eV. The estimated E_g value for Cu-ZnO is 2.63 eV, which exhibits an obvious move in absorption towards the visible region. The decrease in the bandgap of the Cu-ZnO and shifting of its light absorption ability can be ascribed to the sp–d exchange interplay between the confined d electrons of the doped Cu atoms and ZnO electrons.[19] A similar trend is followed by the Cu-ZnO/g-C_3N_4 composites and its optical absorption is notably shifted to the visible region with a bandgap of 2.19 eV. The narrow energy bandgap of Cu-ZnO/g-C_3N_4 composite can be ascribed to the effective surface hybridization between g-C_3N_4 and Cu-ZnO, which is in favor of the photocatalytic sterilization under visible-light irradiation. Moreover, in comparison to ZnO, Cu-ZnO and g-C_3N_4, the Cu-ZnO/g-C_3N_4 composites exhibited stronger absorption over a long wavelength (<470 nm) in the visible region. The improved response of the Cu-ZnO/g-C_3N_4 in the visible region comes from the g-C_3N_4 coupling with Cu-ZnO, and their matching energy band gaps which further enables the sterilization capacity.[11]

3.1.6. PL analyses. It is generally believed that lower PL emission intensity implies lower carrier recombination rate and higher photocatalytic activity.[29] The PL spectra of g-C_3N_4, ZnO, Cu-ZnO and Cu-ZnO/g-C_3N_4 samples at the excitation wavelength of 370 nm are presented in Fig. 7. It could be observed that the emission intensity of Cu-ZnO is significantly reduced as compared to ZnO. The reduction in the intensity of PL spectra of Cu-ZnO occurs due to the induction of some trapped states besides the mid-gap causing a long-life of charge carriers.[19] The PL intensity of Cu-ZnO/g-C_3N_4 is far lower than g-C_3N_4, ZnO and Cu-ZnO, revealing that the e–h pair recombination is prohibited due to the strong interaction and synergistic effect between Cu-

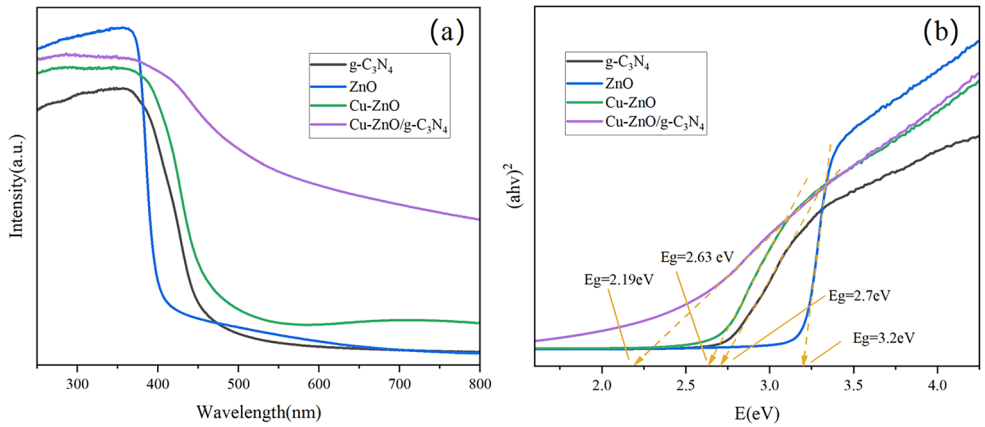

Fig. 6 (a) UV-vis DRS spectra and (b) Tauc Plots of ZnO, Cu-ZnO, g-C_3N_4 and Cu-ZnO/g-C_3N_4 composites.

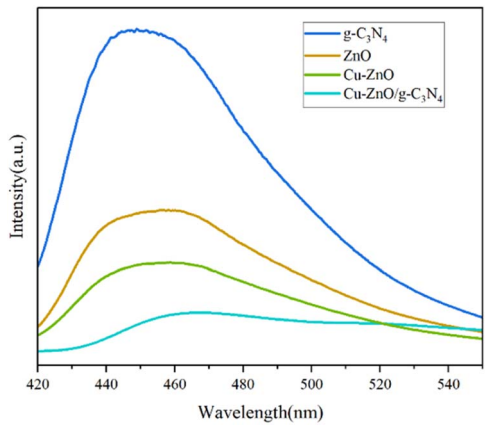

Fig. 7 PL spectra of ZnO, Cu-ZnO, g-C_3N_4 and Cu-ZnO/g-C_3N_4 composites.

ZnO and g-C_3N_4.[16,30] Therefore, the ternary composite is expected to achieve the maximum photocatalytic activity compared to the individual ones.

3.2. Antibacterial activity of Cu-ZnO/g-C_3N_4 composites

3.2.1. Photocatalytic inactivation. Fig. 8(a) shows the survival rate of the ZnO, Cu-ZnO, g-C_3N_4, ZnO/g-C_3N_4 and Cu-ZnO/g-C_3N_4 towards *P. aeruginosa*. Obviously, the cell density of the blank control group did not change significantly, indicating that neither visible light irradiation nor the sterilized PBS had any toxic effect on the bacterial cells. In addition, all photocatalysts exhibited good photocatalytic disinfection performances when irradiated by visible light. The antibacterial capacity of the synthesized photocatalysts can be ordered as follows: g-C_3N_4 < ZnO < Cu-ZnO < ZnO/g-C_3N_4 < Cu-ZnO/g-C_3N_4. It is investigated that the photocatalytic activity of Cu-ZnO is enhanced compared with bare ZnO. Interestingly, further enhancement in the photocatalytic activity is observed for the Cu-ZnO/g-C_3N_4 photocatalyst which could kill almost all *E. coli*, *S. aureus* and *P. aeruginosa* in 60 min. This is attributed to the improved light absorption *via* doping Cu and enhanced charge carrier's separation and transfer *via* coupling g-C_3N_4.

Fig. 8(b) shows the antibacterial rate of Cu-ZnO/g-C_3N_4 towards *E. coli*, *S. aureus* and *P. aeruginosa*. Under light conditions, the antibacterial rates of the Cu-ZnO/g-C_3N_4 composites against *E. coli*, *S. aureus* and *P. aeruginosa* are 99.98%, 99.99%

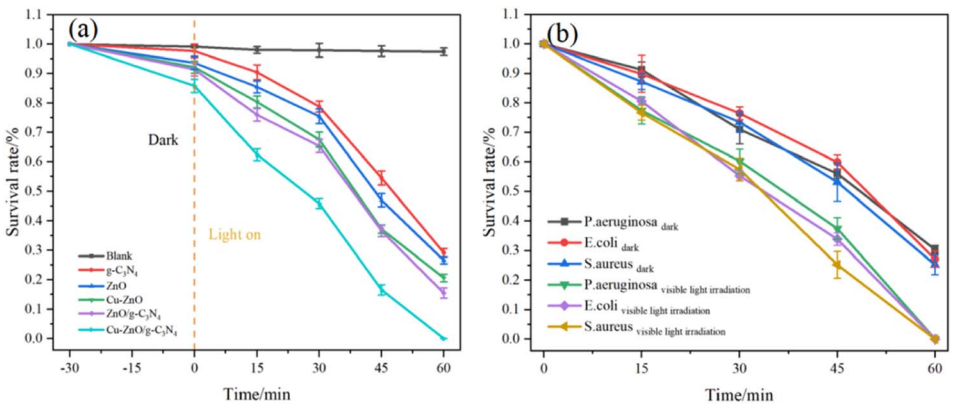

Fig. 8 (a) Survival rate of the photocatalysts towards *P. aeruginosa* and (b) antibacterial rate of Cu-ZnO/g-C_3N_4 towards *E. coli*, *S. aureus* and *P. aeruginosa*.

and 99.93%, respectively. However, Cu-ZnO/g-C_3N_4 has a certain bactericidal efficiency even in the dark, and the bactericidal rates of *E. coli*, *S. aureus* and *P. aeruginosa* are 72.82%, 74.76% and 69.62%, respectively. The large number of bacteria deaths in the dark perhaps comes from Zn^{2+} and Cu^{2+} ions released from the Cu-ZnO/g-C_3N_4 solid solution.[31] It has been reported that Zn^{2+} and Cu^{2+} are able to enter the bacterial cells and disrupt their electron transfer system thereby reducing the expression of enzymes and protein genes and thus resulting in a targeted antibacterial effect.[32]

3.2.2. Stability and reusability. The reusability and stability of the photocatalyst are also important factors in the practical application. In order to estimate the photochemical stability of Cu-ZnO/g-C_3N_4 heterojunction, recycled tests of photocatalytic inactivation of *P. aeruginosa* were conducted. As observed from Fig. 9(a), the photocatalytic performance of the Cu-ZnO/g-C_3N_4 decreases slightly after seven cycles of experiments, and the bactericidal rate for *P. aeruginosa* remained above 98%, illustrating the good reusability of Cu-ZnO/g-C_3N_4 composite in photocatalytic reaction. In addition, the crystal structure and surface functional groups of Cu-ZnO/g-C_3N_4 after seven repeating tests were analyzed by XRD and FTIR. As shown in Fig. 9(b), the XRD pattern displays no evident change in both peak intensity and position, involving all characteristic peaks of ZnO and g-C_3N_4. As seen from Fig. 9(c), the infrared spectrum of the Cu-ZnO/g-C_3N_4 does not change significantly after several cycles. This indicates that the surface functional groups of the Cu-ZnO/g-C_3N_4 remain consistent before and after the cycle which demonstrated the good reusability and high stability of Cu-ZnO/g-C_3N_4 composites.

3.3. Antibacterial activity of Cu-ZnO/g-C_3N_4 cement mortars

Fig. 10 shows the bacterial survival rate of *P. aeruginosa* in CM-0, CM-0.6, CM-1.2 and CM-1.8 mortar samples as the function of time. The CM-0 mortar samples shows a bactericidal rate about 35% against *P. aeruginosa*. This can be explained by the fact that cement mortar as a typical porous material with internal alkaline environment, has certain adsorption and bactericidal effects on bacteria.[33] In this study, the photocatalytic bactericidal ability of mortar samples is in the order: CM-1.8 > CM-1.2 > CM-0.6 > CM-0. Among them, CM-1.8 mortar has the highest bactericidal efficiency to *P. aeruginosa*, which can reach 99.98%.

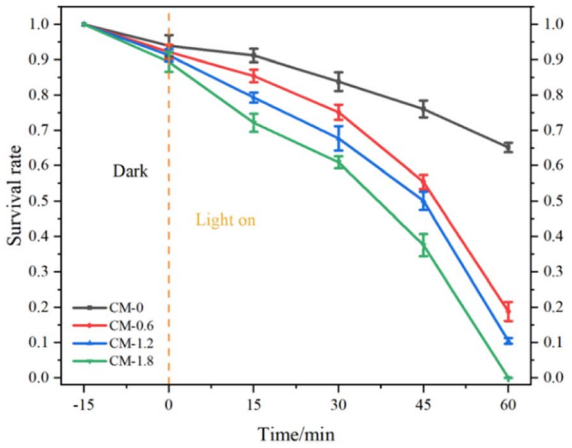

Fig. 10 Survival rate of *P. aeruginosa* in CM-0, CM-0.6, CM-1.2 and CM-1.8 mortar samples as the function of time.

When the content of Cu-ZnO/g-C_3N_4 is lower, the photocatalytic active site exposed on the surface of the mortar is less, and the high alkaline environment inside the mortar reduces the photocatalytic activity of Cu-ZnO/g-C_3N_4. Therefore, the photocatalytic sterilization rate of CM-0.6 mortar is only 81.14%. When the content of Cu-ZnO/g-C_3N_4 is 1.2%, the surface of CM-1.2 mortar specimen is exposed to more photocatalyst material than CM-0.6 mortar, which is conducive to contact between Cu-ZnO/g-C_3N_4 photocatalyst and target bacteria. Therefore, CM-1.2 shows a higher bactericidal rate. The loss of cell viability is directly related to the duration of light exposure, and a longer light duration corresponds to a lower survival rate. At different stages of photocatalytic reaction, it should be noted that the initial steps of photocatalytic inactivation is slow, followed by a faster process of bacterial inactivation. This is mainly due to the fact that the cell wall and plasma membrane are the initial targets of photocatalytic generation of reactive oxygen species (ROS). Due to the complex structure of these initial targets, this process requires a certain amount of cumulative damage and involves more free radicals.[34,35] Therefore, the first step need take a relatively long time resulting in a significant delay in the bacterial inactivation spectrum. When oxidative damage is sufficient to destroy the cell wall and membrane, intracellular contents begin to flow rapidly out of the cells leading to a rapid

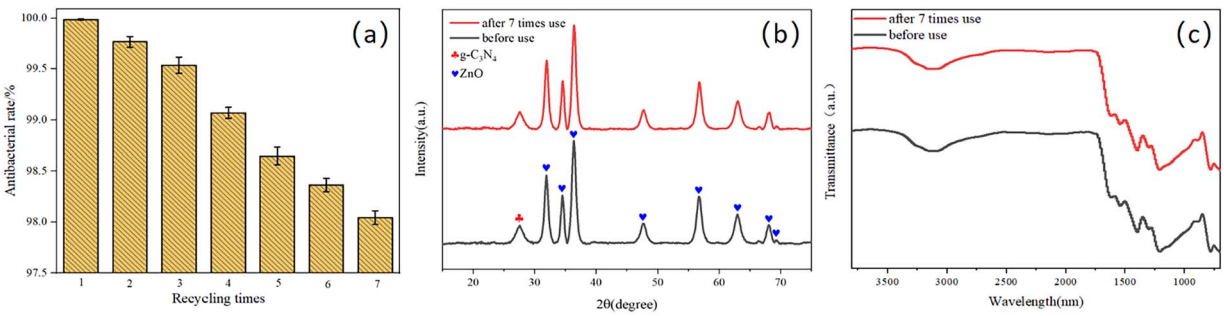

Fig. 9 (a) Recycled photocatalytic inactivation experiments of Cu-ZnO/g-C_3N_4 composites towards *P. aeruginosa*; (b) XRD pattern, (c) FTIR spectra of Cu-ZnO/g-C_3N_4 composites after seven recycled experiments.

loss of cell viability. Another possible explanation is that it could be related to mass transfer effect that affects the initial attachment of bacteria to cementitious surfaces. From a microscopic perspective, most of the Cu-ZnO/g-C_3N_4 can be fixed into cementitious substrates, which greatly limits the diffusion of bacteria from the active sites in the pores on the cementitious surface.[36]

3.4. Sterilization mechanism

Usually, reactive oxygen species (ROS) such as O_2^-, H_2O_2, $^{\cdot}OH$, e^-, and h^+ are responsible for the bactericidal activity during photocatalytic disinfection processes.[37–40] Thus, the trapping experiments were performed to investigate the roles of each reactive species in the photocatalytic disinfection against *P. aeruginosa* over Cu-ZnO/g-C_3N_4 heterostructure. BQ, IPA and sodium oxalate were selected as the scavengers of O_2^-, $\cdot OH$ and h^+ respectively, and the bactericidal experiment without trapping agent was used as the control. As observed from Fig. 11, the photocatalytically bactericidal efficiency is affected to varying degrees when three kinds of capture agents are added, among which the most affecting agent is BQ and sodium oxalate. Obviously, the active substances that played the main role in the reaction were h^+ and O_2^-. But the role of $^{\cdot}OH$ could not be ignored. In addition, the controlled experiments showed that the free radical capture agent had little toxicity to *P. aeruginosa*.

To elucidate the antibacterial mechanism of photocatalysis, photocatalytic antibacterial process of Cu-ZnO/g-C_3N_4 composite was proposed and shown in Fig. 12. As can be seen from Fig. 12, upon the absorption of visible-light photons, electrons in Cu-ZnO/g-C_3N_4 migrate to the conduction band (CB) from the valence band (VB), leaving the holes in CB. Then H_2O reacts with these holes to generate $^{\cdot}OH$, and meantime, the surrounding O_2 reacts with the electrons to produce O_2^-.[21,41] On one hand, the porous and rough structure of the Cu-ZnO/g-C_3N_4 surface allow for bacterial capture and anchoring. The sharp zinc oxide nanosheets can be used for mechanical destruction of cell membranes, while the generated ROS (O_2^-, $^{\cdot}OH$ and h^+) could destroy the bacterial cell components (cell wall, membrane, proteins, DNA, RNA, ribosomes, *etc.*), resulting in membrane disruption and cell death.[42] On the other hand, the

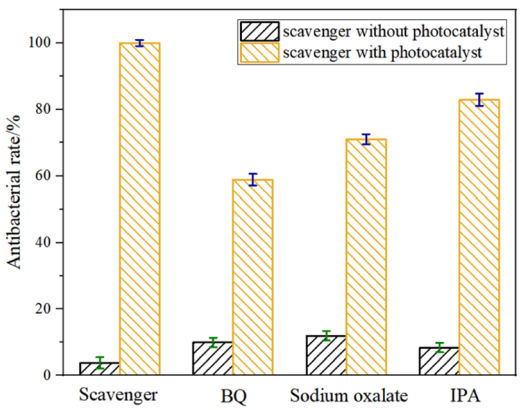

Fig. 11 Effect of BQ, sodium oxalate and IPA on photocatalytic inactivation of Cu-ZnO/g-C_3N_4 towards *P. aeruginosa*.

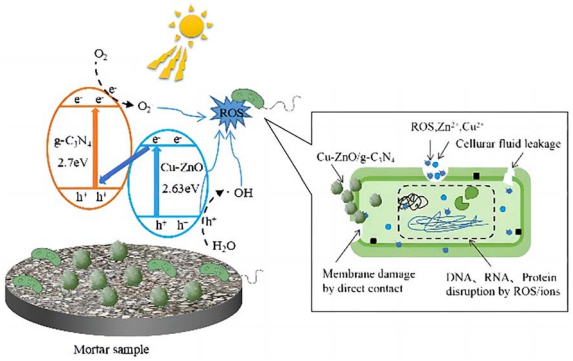

Fig. 12 Schematic illustration of the possible antibacterial mechanism of Cu-ZnO/g-C_3N_4 in mortar samples.

dissolved Zn^{2+} and Cu^{2+} ions from Cu-ZnO/g-C_3N_4 can interact with intracellular contents, and damage the cell membrane.[32,43,44] Although the Zn^{2+} and Cu^{2+} ions were dissolved from the Cu-ZnO/g-C_3N_4 during the soaking process in the aqueous solution, it can be seen from the reusability stability of the photocatalyst after antibacterial experiment (Fig. 9) that the dissolution of both ions did not cause critical stability issue. Thus, Cu-ZnO/g-C_3N_4 still exhibit antibacterial activity in the dark condition (Fig. 8(b)). Generally, factors including, strong visible absorption owing to the suitable bandgap, large specific surface area, ROS generation, as well as the dissolved Zn^{2+} and Cu^{2+} coordinatively contribute to the excellent visible light photocatalytic antibacterial properties of the Cu-ZnO/g-C_3N_4.

4. Conclusions

A hybrid Cu-ZnO/g-C_3N_4 composite was successfully synthesized and introduced to fabricate photocatalytic cement mortars by internal mixing. The photocatalytic activities of prepared composites and the corresponding mortars were evaluated based on bactericidal experiments under visible light. Photocatalytic tests showed that Cu-ZnO/g-C_3N_4 exhibited the strongest photocatalytic bactericidal ability as well as sound performance under dark conditions compared with the ZnO, Cu-ZnO, g-C_3N_4 and ZnO/g-C_3N_4. In addition, Cu-ZnO/g-C_3N_4 showed a high stability in the recycled tests, benefiting for a longtime usage. The photocatalytic cement mortar containing different contents of Cu-ZnO/g-C_3N_4 showed different degrees of photocatalytic germicidal ability, and the germicidal efficiency increased with the increase content of Cu-ZnO/g-C_3N_4. Of note, the antibacterial activity of Cu-ZnO/g-C_3N_4 can be derived from the ROS produced by photocatalysis, which distorts and ruptures the cell membrane. Additionally, the dissolved Zn^{2+} and Cu^{2+} ions from Cu-ZnO/g-C_3N_4 can also interact with intracellular contents, and damage the cell membranes. Consequently, the Cu-ZnO/g-C_3N_4 exhibit antibacterial activity even under the dark conditions.

Author contributions

Xiaomin Liu: data curation, investigation, methodology, software, visualization, writing-original draft; Zhengxian Yang:

conceptualization, supervision, project administration, funding acquisition, writing-review & editing; Kang Li: investigation, visualization, formal analysis; Bruno Briseghella: validation, funding acquisition, writing-review & editing; Giuseppe Carlo Marano: validation, supervision; and Jiankun Xu: methodology, validation, writing-review & editing.

Conflicts of interest

There are no conflicts to declare.

Acknowledgements

This work was financially supported by Fujian Ocean and Fishery Bureau (FJHJF-L-2022-19), Fuzhou Science and Technology Bureau (2021-P-031), and Natural Science Foundation of China (51978171).

References

1 M. Harilal, B. Anandkumar, B. B. Lahiri, R. P. George, J. Philip and S. K. Albert, *Int. Biodeterior. Biodegrad.*, 2020, **155**, 105088.
2 C. D. Parker, *Sewage Ind. Wastes*, 1951, **23**, 1477–1485.
3 J. Peng, J. Zhang and J. Qu, *J. Wuhan Univ. Technol., Mater. Sci. Ed.*, 2006, **21**, 158–161.
4 P. Sikora, K. Cendrowski, A. Markowska-Szczupak, E. Horszczaruk and E. Mijowska, *Constr. Build. Mater.*, 2017, 738–746.
5 B. A. Dehkordi, M. R. Nilforoushan, N. Talebian and M. Tayebi, *Mater. Res. Express*, 2021, **150**, 035403.
6 J. Chen and C. Poon, *Environ. Sci. Technol.*, 2009, **43**, 8948–8952.
7 T. V. Reshma, M. Manjunatha, A. Bharath, R. B. Tangadagi, J. Vengala and L. R. Manjunatha, *Materialia*, 2021, **18**, 1529–2589.
8 M. C. U. Lopez, M. A. A. Lemus, M. C. Hidalgo, R. L. Gonzalez, P. Q. Owen, S. A. U. Lopez and J. Acosta, *J. Nanomaterials*, 2019, **2019**, 1015876.
9 A. M. Tama, S. Das, S. Dutta, M. D. I. Bhuyan and M. N. I. A. Basith, *RSC Adv.*, 2019, **9**, 40357–40367.
10 V. Vaiano, G. Iervolino and L. Rizzo, *Appl. Catal., B*, 2018, **238**, 471–479.
11 I. Ahmad, *Sep. Purif. Technol.*, 2020, **251**, 117372.
12 M. Huang, Z. Yang, L. Lu, J. Xu, W. Wang and C. Yang, *Catalysts*, 2022, **12**, 443.
13 B. Chai, T. Peng, J. Mao, K. Li and L. Zan, *Phys. Chem. Chem. Phys.*, 2012, **14**, 16745–16752.
14 Z. Wang, W. Guan, Y. Sun, F. Dong, Y. Zhou and W. Ho, *Nanoscale*, 2015, **17**, 2471–2479.
15 W. Jo and N. C. S. Selvam, *J. Hazard. Mater.*, 2015, **299**, 462–470.
16 S. Ma, S. Zhan, Y. Xia, P. Wang, Q. Hou and Q. Zhou, *Catal. Today*, 2019, **330**, 179–188.
17 N. Nie, F. He, L. Zhang and B. Cheng, *Appl. Surf. Sci.*, 2018, **457**, 1096–1102.
18 X. Zhang, J. Zhang, J. Yu, Y. Zhang, Z. Cui, Y. Sun and B. Hou, *Appl. Catal., B*, 2018, **220**, 57–66.
19 M. A. Qamar, S. Shahid, M. Javed, S. Iqbal, M. Sher and M. B. Akbar, *J. Photochem. Photobiol., A*, 2020, **401**, 112776.
20 K. V. A. Kumar, S. R. Amanchi and B. Sreedhar, *RSC Adv.*, 2017, **7**, 43030–43039.
21 N. T. T. Truc, D. S. Duc, D. V. Thuan, T. A. Tahtamouni, T. D. Pham, N. T. Hanh, D. T. Tran, M. V. Nguyen, N. M. Dang, N. T. P. Le Chi and V. N. Nguyen, *Appl. Surf. Sci.*, 2019, **489**, 875–882.
22 S. P. Adhikari, H. R. Pant, J. H. Kim, H. J. Kim, C. H. Park and C. S. Kim, *Colloids Surf., A*, 2015, **482**, 477–484.
23 E. Jang, D. W. Kim, S. H. Hong, Y. M. Park and T. J. Park, *Appl. Surf. Sci.*, 2019, **487**, 206–210.
24 H. Li, M. Ding, L. Luo, G. Yang, F. Shi and Y. Huo, *ChemCatChem*, 2020, **12**, 1334–1340.
25 L. Ge and C. Han, *Appl. Catal., B*, 2012, **117**, 268–274.
26 M. Sher, S. Shahid and M. Javed, *J. Photochem. Photobiol., B*, 2021, **219**, 112202.
27 Y. Zhou, L. Zhang, W. Huang, Q. Kong, X. Fan, M. Wang and J. Shi, *Carbon*, 2016, **99**, 111–117.
28 N. Kumaresan, M. M. A. Sinthiya, M. Sarathbavan, K. Ramamurthi, K. Sethuraman and R. R. Babu, *Sep. Purif. Technol.*, 2020, **244**, 116356.
29 W. Jo, S. Kumar, P. Yadav and S. Tonda, *Appl. Surf. Sci.*, 2018, **445**, 555–562.
30 Q. T. H. Ta, G. Namgung and J. Noh, *J. Photochem. Photobiol., A*, 2019, **118**, 110–119.
31 B. Leng, X. Zhang, S. Chen, J. Li, Z. Sun, Z. Ma, W. Yang, B. Zhang, K. Yang and S. Guo, *J. Mater. Sci. Technol.*, 2021, **94**, 67–76.
32 C. Su, A. K. Berekute and K. Yu, *Sustainable Environ. Res.*, 2022, **32**, 27.
33 T. Guan, L. Fang, Y. Lu, F. Wu, F. Ling, J. Gao, B. Hu, F. Meng and X. Jin, *Colloid. Surface. A*, 2017, **529**, 907–915.
34 K. Sunda, T. Watanabe and K. Hashimoto, *J. Photochem. Photobiol., A*, 2003, **156**, 227.
35 J. Marugan, V. G. Rafael, C. Pablos and C. Sordo, *Water Res.*, 2010, **44**, 789–796.
36 E. Rokhsat and O. Akhavan, *Appl. Surf. Sci.*, 2016, **371**, 590–595.
37 K. Qi, B. Cheng, J. Yu and W. Ho, *J. Alloy. Compd.*, 2017, **727**, 792–820.
38 H. Shi, C. Wang, W. Wang, X. Hu, J. Fan and Z. Tang, *Ceram. Int.*, 2021, **47**, 7974–7984.
39 D. Pancholi, N. S. Bisht, V. Pande and A. Dandapat, *Colloids and surfaces. B, Biointerfaces*, 2021, **199**, 111558.
40 E. Rokhsat and O. Akhavan, *Appl. Surf. Sci.*, 2016, **371**, 590–595.
41 Y. Zhang, P. Ju, L. Hao, X. Zhai, F. Jiang and C. Sun, *J. Alloys Compd.*, 2021, 157224.
42 P. K. Stoimenov, R. L. Klinger, G. L. Marchin and K. J. Klabunde, *Langmuir*, 2002, **18**, 6679–6686.
43 A. Awad, A. I. Abou-Kandil, I. Elsabbagh, M. Elfass, M. Gaafar and E. Mwafy, *J. Thermoplast. Compos. Mater.*, 2015, **28**, 1343–1358.
44 X. Bellanger, P. Billard, R. E. L. Schneider, L. Balan and C. Merlin, *J. Hazard. Mater.*, 2015, **283**, 110–116.